Check for updates

Tunable microscopic aggregation morphology of α-Ni(OH)₂ for enhanced photocatalytic degradation of fracturing flowback fluid with ozone synergy

Huohai Yang[1], Xinrui Tang[1], Renze Li[1]*, Xuanyu Liu[1], Ping Zhang[2] and Yeqi Gong[1]

[1]School of Petroleum Engineering, Southwest Petroleum University, Chengdu, China, [2]West-East Gas Transmission Branch of State Pipeline Group United Pipeline Co., Shanghai, China

In this study, hydrothermal synthesis was used to prepare α-Ni(OH)₂, which is a steady-state photocatalytic material. Furthermore, ball milling was used for the 1:1 loading of α-Ni(OH)₂ with nano-alumina (Al₂O₃), hexagonal boron nitride (h-BN), and activated carbon (AC). The performances of these four materials in the degradation of a fracturing flowback fluid were investigated under the synergistic catalytic effect of ozone. The results showed that under this effect, the α-Ni(OH)₂/nano -Al₂O₃ photocatalyzed the formation of active hydroxyl radicals (·OH) and superoxide radicals (·O₂⁻), which in turn degraded the return solution. Although ozone itself can spontaneously form certain ·OH and O₂⁻ in water, compared to α-Ni(OH)₂, the nano- Al₂O₃ with a higher valence band of 0.2eV provided more active sites and better electron migration efficiency for the conversion of ozone, improving the conversion efficiency of this process (Figure 11). In addition, unlike the other two types of carriers, nano-Al₂O₃ could provide intergranular support for nanopillared α-Ni(OH)₂, increasing the specific surface area and the number of active sites.

KEYWORDS

α-Ni(OH)₂, hydroxypropyl gum fracturing flowback fluid, ozone, photocatalytic, synergistic catalysis

Introduction

Hydraulic fracturing is an important conventional technique for oil extraction that can boost production and injection (Li et al., 2016; You et al., 2018). However, hydraulic fracturing typically generates a large amount of fracturing flowback fluid (Liu et al., 2010; Aminto and Olson, 2012), which severely impacts the environment and ecological safety. This fracturing flowback fluid is mainly composed of the fracturing fluid, followed by the fungicides, pH stabilizers, suspended gum substances, and gel breakers used in oil

TABLE 1 The characteristics of similar reported catalysts.

Materials	Characteristics	Degradation mechanism
TiO_2	1 Wide band gap 2 Requires high-energy UV excitation 3 No efficient use of solar energy 4 Low photogenerated electron and hole complex efficiency	Activated electron–hole pairs and catalyzed oxidation
α-$Ni(OH)_2$/TiO_2 (Yu et al., 2011)	1 α-$Ni(OH)_2$ as a co-catalyst 2 The synthesis and loading of α-$Ni(OH)_2$/TiO_2 at room temperature was reported for the first time	The potential of Ni 2p was slightly lower than the conduction band of TiO_2, while it was higher than the reduction potential of H_2, assisting in the charge separation
α-$Ni(OH)_2$/TiO_2 (Yan et al., 2014)	1 The optimal molar ratio of α-$Ni(OH)_2$/TiO_2 was determined 2 The performance of α-$Ni(OH)_2$ as a co-catalyst was superior to those of CoO_x, $Co(OH)_2$, NiO_x, $Fe(OH)_3$, and $Cu(OH)_2$	
TiO_2/α-$Ni(OH)_2$ (Meng et al., 2018)	Successful preparation of layered composites with a thickness of 20 nm uniformly spread onto the surface of TiO_2 fibers by a simple wet chemical precipitation method	In addition to enhanced charge separation efficiency, the CO_2 capture capacity was also improved
α-$Ni(OH)_2$/CdS (Ran et al., 2011)	1 The loading of α-$Ni(OH)_2$ modified CdS nanorods in composites at room temperature was reported for the first time 2 The optimal load ratio was determined	The potential of Ni^{2+} was more negative than the conduction band of CdS, while higher than the reduction potential of H_2, assisting in the charge separation
α-$Ni(OH)_2$ (Zhang et al., 2021)	1 Adjusting the layer spacing of α-$Ni(OH)_2$ by changing the solvent 2 No toxic NO_2 by-products were generated	By adjusting the layer spacing, the specific surface area and number of active sites were increased, new reaction routes were provided, the activation of surface adsorbents was enhanced, and the production of toxic NO_2 by-products was completely prevented
$Zn_{0.5}Cd_{0.5}S$/$Ni(OH)_2$ (Gao et al., 2021)	Use of homogeneous zinc cadmium sulfide ($Zn_{0.5}Cd_{0.5}S$) nanoparticles instead of CdS with severe corrosion, with phosphorus as the primary catalyst	An intimate two-dimensional (2D)/zero-dimensional (0D) heterojunction was formed
$BiOBr_xI_{1-x}$/BiOBr (Shi et al., 2018; Shi et al., 2019a; Shi et al., 2019b)	$BiOBr_xI_{1-x}$ solid solution coupling with the BiOBr monomer as a heterojunction structural photocatalyst	An enhanced exciton photocatalysis effect was induced by the solid solution structure, and an enhanced carrier photocatalysis effect was induced by the complex structure
Ag_2O/TiO_2 (Chen et al., 2020)	Clarified how two different phases of Ag_2O play a role in enhancing visible light photocatalytic performance	The surface plasmon resonance (SPR) effect of metallic Ag could favor electron transfer to the conduction band of TiO_2
$Sr_{1.36}Sb_2O_6$ $Sr_2Sb_2O_7$ (Huang et al., 2021)	The application and mechanism of the effect of $Sr_{1.36}Sb_2O_6$ and $Sr_2Sb_2O_7$ in TC degradation were explored for the first time	The different photocatalytic activities observed for $Sr_{1.36}Sb_2O_6$ and $Sr_2Sb_2O_7$ could be attributed to their different electronic and crystal structures
$AgNbO_3$/Fe_2O_3 (Chang et al., 2021)	A new material for the photocatalytic decomposition of PVC-($AgNbO_3$/Fe_2O_3) was prepared, and its photocatalytic degradation characteristics were investigated	An appropriate amount of Fe_3O_2 inhibited the recombination of electrons and holes. Fe^{3+} was reduced to Fe^{2+} during excitation, and Fe^{2+} might have reacted with H_2O_2 to produce $\cdot$OH.

extraction. The treatment requirements for the fracturing flowback fluid in the oil and gas fields at home and abroad are mainly designed to meet the discharge and re-injection standards. The methods used include physical, chemical, biological, and combined processes. These methods face challenges of complexity and high costs.

Photocatalytic technology has been successfully applied for environmental improvement and has good application prospects in the degradation of organic pollutants in water bodies (Carp et al., 2004; Ahmed, 2012; Fu et al., 2019). The development of new visible-light photocatalysts has always been a major research focus (Mutalib et al., 2018; Lee et al., 2022; Nien et al., 2022). $Ni(OH)_2$ has been used for electrode material in batteries (Tretyachenko et al., 2014). Based on the layer spacing and intercalated particles, nickel hydroxide can be mainly classified into α-$Ni(OH)_2$ and β-$Ni(OH)_2$ crystalline structures (Lee et al., 2011; Li et al., 2015). The adjacent layers of β-$Ni(OH)_2$ are closely packed, whereas the crystals of α-$Ni(OH)_2$ have a defect structure and are good p-semiconductors, which makes it easier for foreign anions to intercalate into the layers of α-$Ni(OH)_2$ (Hall et al., 2015). However, $Ni(OH)_2$ is no longer limited to experiments studying cells and corrosion processes. Today, $Ni(OH)_2$ and its composites are used in various practical applications, including photocatalysis (Ran et al., 2011; Yu et al., 2011; Yan et al., 2014; Meng et al., 2018; Shi et al., 2018; Shi et al., 2019a; Shi et al., 2019b; Chen et al., 2020; Chang et al., 2021; Gao et al., 2021; Huang et al., 2021; Zhang et al., 2021) (Table 1).

In this study, α-$Ni(OH)_2$ was synthesized using a hydrothermal synthesis method, and then ball milling was used to load it with three conventional photocatalysts. XRD, XPS, DRS, SEM, FTIR, BTE, Raman spectroscopy, and other characterization methods were used to determine its basic

structure. Subsequently, ozone was used to synergistically enhance the catalytic performance of α-Ni(OH)$_2$. Because of the field demand for hydraulic fracturing, experiments on the photocatalytic treatment of the fracturing flowback fluid were conducted, and the effects of α-Ni(OH)$_2$ and its composites on real fracturing flowback fluid containing polymers were evaluated (Figure 1).

Materials and methods

Synthesis methods for α-Ni(OH)$_2$ and its composites

The hydrothermal synthesis method was used to synthesize α-Ni(OH)$_2$. First, 0.452 g of urea and 0.5436 g of nickel nitrate were dissolved in 30 ml of solvent (water), stirred for 30 min, completely dissolved, and then transferred to a reactor. The reactor was placed in an electrothermostatic blast oven and maintained at 120°C for 4 h. The reactor was then removed and cooled naturally for 1.5 h, followed by centrifugal washing with anhydrous ethanol several times (water and ethanol cross-washing six times), followed by centrifugation at 5000 rpm for 3 min. The samples were dried and kept warm in a vacuum-drying oven at 50°C. Finally, the obtained green powder sample was α-Ni(OH)$_2$.

The synthesized α-Ni(OH)$_2$ composites were obtained by mixing 3 g of nano-alumina, hexagonal boron nitride, or activated carbon (AC) powder and 3 g of α-Ni(OH)$_2$ powder and placing these mixtures in agate jars with different sizes of agate balls for ball milling. The ball mill was set at 250 rpm for 30 min. Finally, the mixed powder was collected from each ball mill jar, placed in a blast drying oven at 90°C, and dried for 6 h to prepare samples of nano-alumina-loaded α-Ni(OH)$_2$, hexagonal boron nitride-loaded α-Ni(OH)$_2$, and activated carbon-loaded α-Ni(OH)$_2$ as composite photocatalytic materials.

Compositions of simulated fluid and actual fracturing flowback fluid

In this study, hydroxypropyl gum with ammonium persulfate as a gel breaker was used as a simulated flowback fluid for treatment in a photocatalytic-environment study. The performance evaluation of the self-synthesized photocatalyst was carried out using a fracturing flowback fluid provided by a fracturing site in the Sulige gas field, China. The fracturing fluid agent applied during hydraulic fracturing was formulated as follows: 0.5% hydroxypropyl gum, 0.02% pH adjuster, 1.0% demulsifier, 1.0% cleanup additive, 0.5% temperature stabilizer, 1.0% clay stabilizer, and 6% organic boron crosslinking agent (crosslinking ratio of 10:1).

Results and discussion

Structure, morphology, and optical properties of α-Ni(OH)$_2$ and its composites

To study the microstructures of the different samples, the α-Ni(OH)$_2$ and the modified microstructure of the composites were investigated using XRD (Figure 2). The presence of four distinct diffraction peaks ({003},{006},{101}, and {110}) for α-Ni(OH)$_2$, combined with the findings of Zhang et al. (2021), suggests that the basic α-Ni(OH)$_2$ photocatalyst is synthesized with high purity and dominates in the composite.

Second, the position of the {101} diffraction peak for α-Ni(OH)$_2$/nanoAl$_2$O$_3$ is more to the left than that of the {101} diffraction peak for α-Ni(OH)$_2$. This is due to the presence of replacement ions in α-Ni(OH)$_2$/nanoAl$_2$O$_3$ relative to the α-Ni(OH)$_2$ alone, resulting in shifts in the {006} and {101} diffraction peaks, thus confirming the presence of the nanoAl$_2$O$_3$ in the α-Ni(OH)$_2$.

The {003},{101}, and{110} diffraction peak positions for α-Ni(OH)$_2$/h-BN and α-Ni(OH)$_2$/AC are flatter than those for α-Ni(OH)$_2$. There is a strong h-BN characteristic peak on the right side of the {006} diffraction peak position for α-Ni(OH)$_2$/h-BN, indicating that h-BN has a significant influence on α-Ni(OH)$_2$. The {003},{101}, and {110} diffraction peak positions for α-Ni(OH)$_2$/AC are flatter than those for α-Ni(OH)$_2$/h-BN, but the {006} diffraction peak positions for α-Ni(OH)$_2$/AC and α-Ni(OH)$_2$ are consistent, indicating that AC is the best loading for α-Ni(OH)$_2$.

According to the equation: interlayer spacing = interplanar crystal spacing - layer thickness (0.48 nm for α-Ni(OH)$_2$)) (Jia et al., 2017), the interlayer spacing of α-Ni(OH)$_2$ is 0.24 nm. Therefore, the three types of carriers do not affect the α-Ni(OH)$_2$ layer spacing significantly. The layer spacing measured by XRD was the average value, and the three types of carriers may have had local structural effects on α-Ni(OH)$_2$.

SEM was used to observe the structural morphology of the α-Ni(OH)$_2$ and its composites (Figure 3). The microscopic morphology of the α-Ni(OH)$_2$ photocatalyst exhibits a sphere composed of micro-nanopillars, with local agglomeration but a uniform overall dispersion and an average diameter of approximately 1 μm for individual spherical particles (Figure 3A). The α-Ni(OH)$_2$/nano-Al$_2$O$_3$ is dominated by spheres composed of micro-nanopillars supplemented by irregularly shaped nano-sized particles, which are more finely and uniformly dispersed compared to those in the α-Ni(OH)$_2$ alone, with an average diameter of approximately 1 μm for individual spherical particles. The dendritic villi of the spherical particles are attached and fixed to the cotton-like irregular nanoparticles on them, and the microscopic morphology of α-Ni(OH)$_2$ does not change significantly (Figure 3B). The microscopic morphology of the α-Ni(OH)$_2$/h-BN photocatalyst is dominated by the spheres composed of
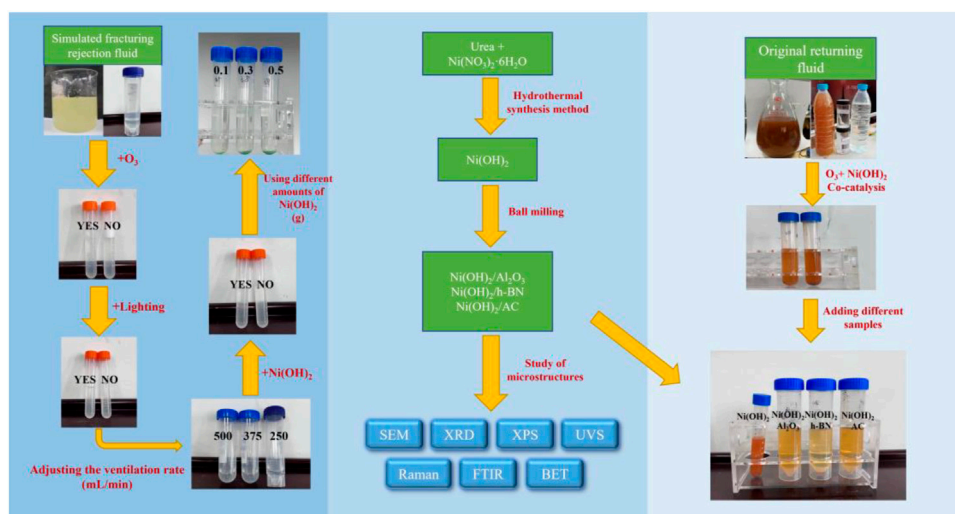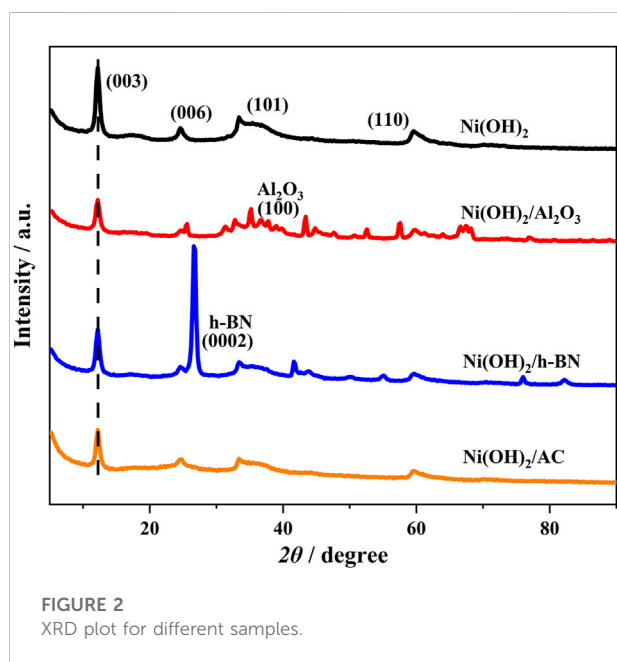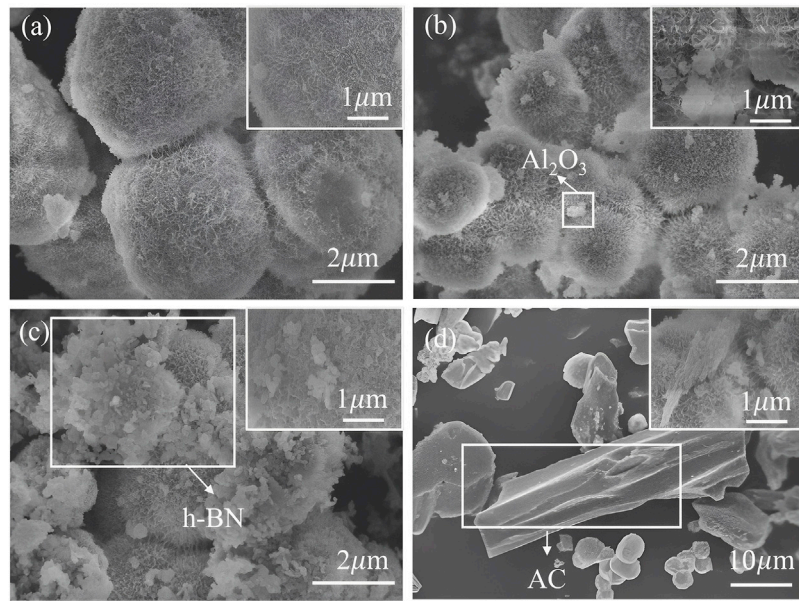
FIGURE 1
Technical processes.

FIGURE 2
XRD plot for different samples.

micro-nanopillars supplemented by pebble-like nano-sized particles, which are more finely dispersed than those in the α-Ni(OH)$_2$ alone, but the agglomeration is more pronounced, with individual spherical particles averaging around 1 μm in diameter. The spherical particles with dendritic villi have a clear attachment, and anchoring relationship to the pebble-like irregular nanoparticles, the surface of the photocatalyst is rougher, and the micromorphology is more complex overall

(Figure 3C). The microscopic morphology of the α-Ni(OH)$_2$/ AC photocatalyst is dominated by a lamellar crystal structure, supplemented by microspheres composed of micro-nanopillars, where the spheres are either adsorbed on the lamellar crystals or dispersed. Compared to the overall dispersion of α-Ni(OH)$_2$, the α-Ni(OH)$_2$/AC agglomeration is more pronounced, with the overall microscopic size becoming approximately an order of magnitude higher, and the average length of the layered crystals is approximately 10 μm, indicating that the compounding of α-Ni(OH)$_2$/AC causes a significant loss in the specific surface area of the α-Ni(OH)$_2$ (Figure 3D).

Figure 4 shows the partial binding energy spectra of α-Ni(OH)$_2$/nano-Al$_2$O$_3$, where the Ni 2p peaks at 856.7 and 862.3 eV are associated with α-Ni(OH)$_2$, as well as its satellite peaks, while the peak at 866.6 eV is associated with Ni^{3+}, along with its satellite peaks (Figure 4A) (Li et al., 2018; Rajendiran et al., 2020). It should be noted that previous studies have confirmed that Ni^{3+} is often the active site for increased catalytic activity (Wang et al., 2015). It is well known that the O1s binding energy of α-Ni(OH)$_2$ is 530.5 eV, which is between 530.0 and 531.5 eV, indicating the presence of the Ni-O and O-H bonds in the hydroxyl group in the α-Ni(OH)$_2$ photocatalyst. The O1s binding energy of the α-Ni(OH)$_2$/nano-Al$_2$O$_3$ photocatalyst is 530.8 eV, which is 0.3 eV higher than that of α-Ni(OH)$_2$, indicating the presence of Al-O bonds, in addition to Ni-O and O-H bonds (Figure 4B). Furthermore, the C 1 s peaks at 284.8 and 289.2 eV originate from C-C and O-C=O bonds (Figure 4D), respectively, which are derived from the precursor urea and had little impact on the accuracy of the catalytic guar glue oxidation.

FIGURE 3
SEM results for **(A)** α-Ni(OH)$_2$, **(B)** α-Ni(OH)$_2$/nano-Al$_2$O$_3$, **(C)** α-Ni(OH)$_2$/h-BN, and **(D)** α-Ni(OH)$_2$/AC.
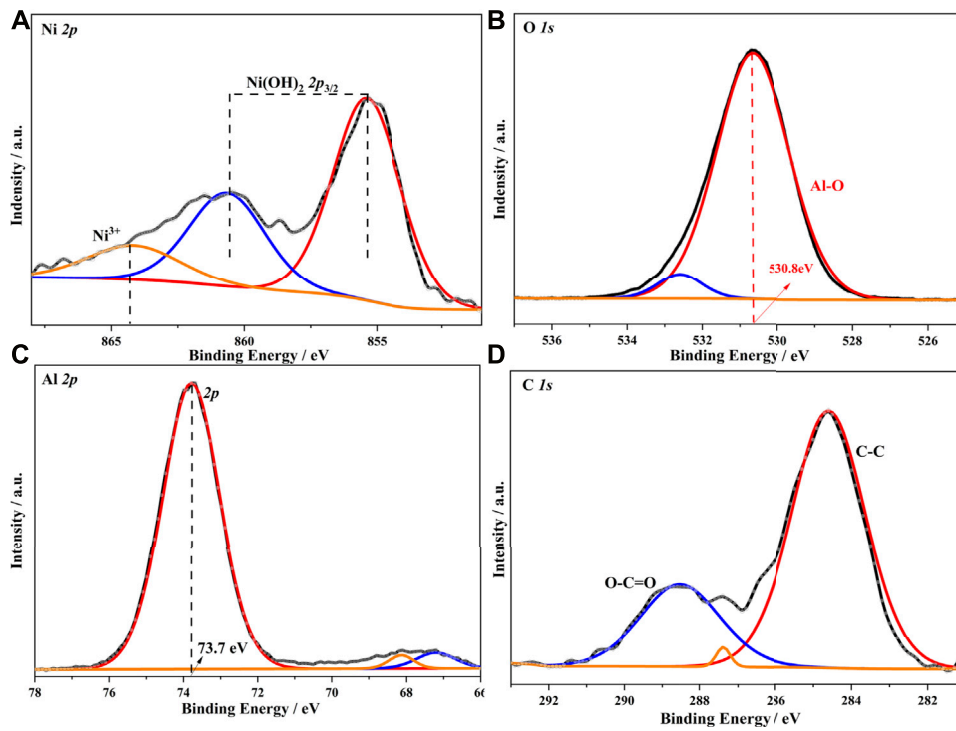
FIGURE 4
Partial binding energy spectra of α-Ni(OH)$_2$/Al$_2$O$_3$ composite: **(A)** α-Ni(OH)$_2$/Al$_2$O$_3$Ni 2 p, **(B)** α-Ni(OH)$_2$/Al$_2$O$_3$ O 1 s, **(C)** α-Ni(OH)$_2$/Al$_2$O$_3$ Al 2 p, and **(D)** α-Ni(OH)$_2$/Al$_2$O$_3$ C 1 s.
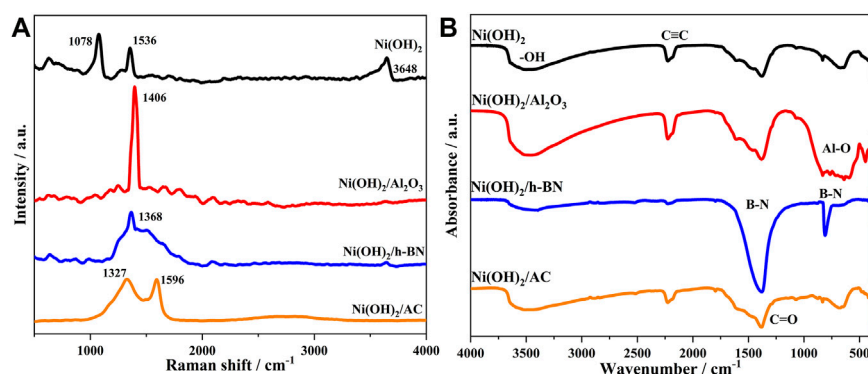
FIGURE 5
(A) Raman spectra of different samples; and **(B)** FTIR spectra of different samples.

The Raman spectra of α-Ni(OH)$_2$ and its composites (Figure 5A) show the presence of characteristic peaks for α-Ni(OH)$_2$ at 1078 and 1536 cm^{-1}, and a characteristic peak for Al$_2$O$_3$ at 1406 cm^{-1}, proving the effective combination of Al$_2$O$_3$ and α-Ni(OH)$_2$. The characteristic peak of α-Ni(OH)$_2$/h-BN at 1368 cm^{-1} is attributed to the E$_{2g}$ vibration mode of h-BN (Mekki et al., 1999); α-Ni(OH)$_2$/AC has two peaks at 1327 and 1596 cm^{-1}, corresponding to the D-band and G-band peaks, respectively, where the D-band peak is caused by the defective carbon crystallites, and the G-band peak was caused by the crystallite graphitization (Li et al., 2019). This indicated that the Ni(OH)$_2$ effectively bound to all three loading materials.

In the FTIR spectra of α-Ni(OH)$_2$ and its composites (Figure 5B), the peak at 3642 cm^{-1} corresponds to the hydroxyl in the Ni(OH)$_2$, and that at 2225 cm^{-1} is attributed to the C-C bond in the urea molecule, the precursor of the synthesized Ni(OH)$_2$. The peak at 1440 cm^{-1} represents the C=O stretching vibration in the AC (Sidiras et al., 2011), and the two strong absorption peaks at 1423 and 809 cm^{-1} are the B-N stretching vibration absorption peak and bending vibration absorption peak for the h-BN particles, respectively (Kim et al., 2014). A wider absorption band at 511 cm^{-1} can correspond to the Al-O bond vibration absorption peak for the Al$_2$O$_3$ fibers, which is a characteristic absorption band of nano-alumina (Dunia et al., 2021). This indicates that α-Ni(OH)$_2$ is effectively bound to all three materials.

Figure 6 shows the nitrogen adsorption–desorption isotherms of α-Ni(OH)$_2$ and its composites. Table 2 lists the structural parameters of the four samples, where the pore volumes of α-Ni(OH)$_2$/AC and α-Ni(OH)$_2$/Al$_2$O$_3$ are relatively large (i.e., 0.52 and 0.28 cm^{3}g^{-1}, respectively). The α-Ni(OH)$_2$, α-Ni(OH)$_2$/Al$_2$O$_3$, α-Ni(OH)$_2$/h-BN, and α-Ni(OH)$_2$/AC have surface areas of 213.35, 138.67, 122.30,
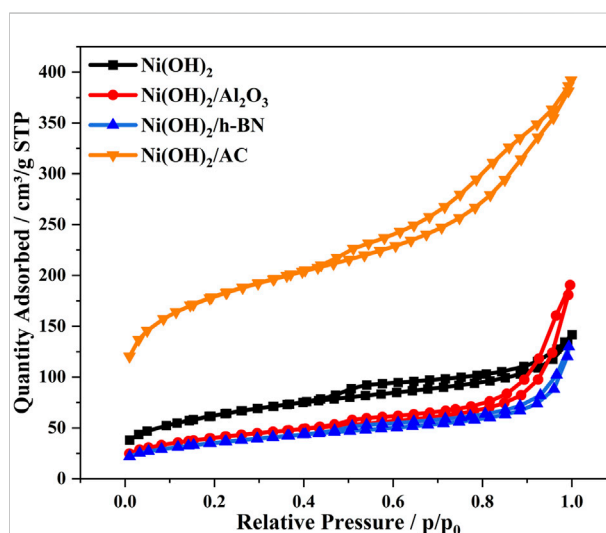
FIGURE 6
N$_2$ adsorption–desorption isotherms of different samples.

and 586.83 m^{2}g^{-1}, respectively. The surface area of α-Ni(OH)$_2$/AC is much higher than those of the other samples, which are analyzed because the AC has a porous structure and a high surface area. The α-Ni(OH)$_2$/Al$_2$O$_3$ and α-Ni(OH)$_2$/h-BN have relatively large pore sizes, mainly concentrated at 10.04 and 7.64 nm, respectively, which are more favorable for the entry of pollutants.

As shown in the UV–vis diffuse reflectance spectra of α-Ni(OH)$_2$ and its composites (Figure 7A), both α-Ni(OH)$_2$ and its composites exhibit strong absorption in the visible range, which proves that these materials can respond positively to the excitation of visible light. Among them, α-Ni(OH)$_2$ has the highest maximum absorption at a visible wavelength of

TABLE 2 Structural parameters of different samples.

Sample	S_{BET} (m^{2}g^{-1})	V_{total} (cm^{3}g^{-1})	Pore size (nm)
α-Ni(OH)$_2$	213.35	0.18	4.41
α-Ni(OH)$_2$-Al$_2$O$_3$	138.67	0.28	10.04
α-Ni(OH)$_2$-BN	122.30	0.20	7.64
α-Ni(OH)$_2$-AC	586.83	0.52	5.06

TABLE 3 Effectiveness of α-Ni(OH)$_2$ and its composites in the degradation of fracturing flowback liquid.

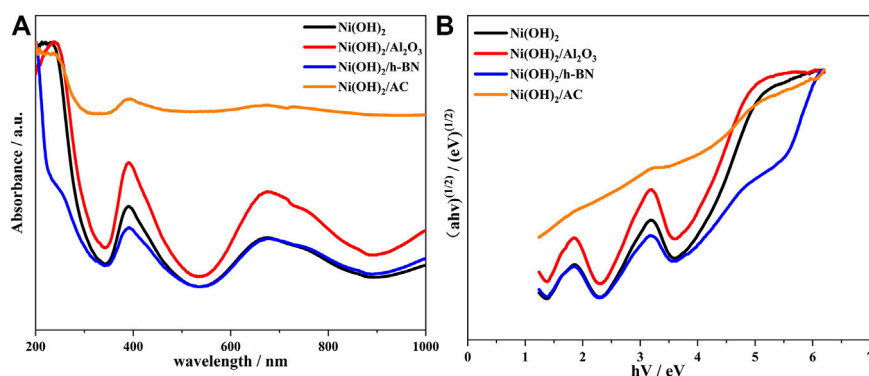| Materials	Gas Flux	Ozone Concentration (ppm)	Illumination
0.1g α-Ni(OH)$_2$	500 ml/min	100	Illuminated
0.1 g α-Ni(OH)$_2$/0.1 g nano-Al$_2$O$_3$	500 ml/min	100	Illuminated
0.1 g α-Ni(OH)$_2$/0.1 g h-BN	500 ml/min	100	Illuminated
0.1 g α-Ni(OH)$_2$/0.1 g AC	500 ml/min	100	Illuminated

FIGURE 7
(A) UV−vis diffuse reflectance spectroscopy results for different samples; and **(B)** band gaps of different samples.

389 nm, followed by that at 676 nm, and the values for the three composites do not differ much from those for the α-Ni(OH)$_2$.

The α-Ni(OH)$_2$ and its composites are indirect band gap semiconductors. Using the equation $\alpha h\nu = A(h\nu - E_g)^{n/2}$, a curve is obtained from the relationship between light absorption coefficient (αhv)1/2 and hv (Figure 7B). The coordinate values of the intersection between the extension of the straight line and the X-axis can be used to determine that the band gap values of the prepared photocatalysts α-Ni(OH)$_2$, α-Ni(OH)$_2$/nanoAl$_2$O$_3$, α-Ni(OH)2/h-BN, and α-Ni(OH)$_2$/ AC are approximately 3.34, 3.33, 3.02, and 1.90 eV, respectively. The test results indicate that the energy band structures of the nano-Al$_2$O$_3$, h-BN, and AC significantly change after loading the α-Ni(OH)$_2$ compared to that with α-Ni(OH)$_2$ alone.

Photocatalytic degradation of hydroxypropyl gum by α-Ni(OH)$_2$ photocatalyst

The factors affecting photocatalytic degradation include the type and dosage of the photocatalyst, the light source, the applied oxidant, and the initial concentration of the reactant. Among these, the applied oxidant can react with photo-induced electrons to reduce the electrons and thus decrease the electron–hole recombination rate, which can increase the degradation rate of the photocatalytic reaction. The oxidant also has a degradation effect on organic matter to some extent (Dhanalakshmi et al., 2008; Yang et al., 2009). In this study, ozone was introduced, and the ozone catalytic oxidation method was adopted to remove the refractory organic matter in the fracturing flowback fluid from the oil field by reacting it with α-Ni(OH)$_2$ to produce ·OH
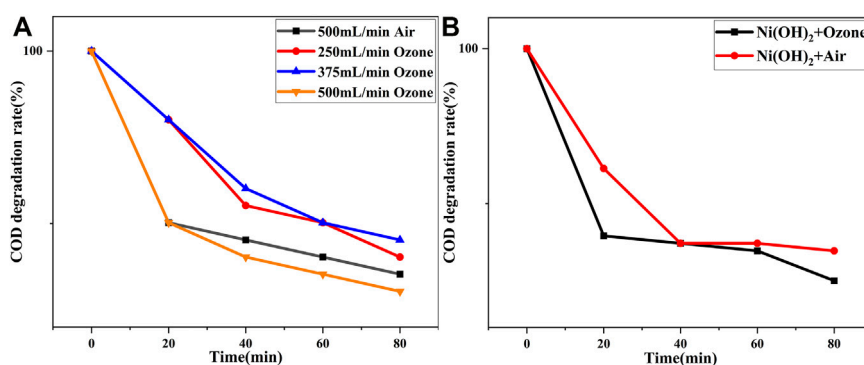
FIGURE 8
(A) Effect of ozone on the degradation of hydroxypropyl gel breaker; and **(B)** effect of ozone on the photocatalytic degradation of α-Ni(OH)$_2$.

(hydroxyl radical) with a stronger oxidizing ability (Agustina et al., 2006; Mohammad et al., 2012).

Therefore, to lay the foundation for the experiment on the photocatalytic degradation activity, this study considered the photocatalytic reaction assisted by ozone and explored the degradation effect of ozone on a hydroxypropyl gel breaker; carried out by comparing the degradations of the hydroxypropyl gel breaker with and without ozone under visible light.

Figure 8A shows that ozone, as a strong oxidizing agent, produced hydroxyl radicals (·OH) and superoxide radicals (·O$_2^-$), which have a slight degradation effect on the hydroxypropyl gel breaker when applied to the liquid alone. It could be concluded that the effect of ozone alone on the degradation of the hydroxypropyl gel breaker is only 1.11%. It is worth noting that reducing the ozone aeration rate reduces the degradation efficiency, proving that although both oxygen and ozone can produce ·OH and ·O$_2^-$, there is no synergistic degradation, and the degradation efficiency is poor without the adsorption and activation of the photocatalyst.

Figure 8B shows that ozone, as a strong oxidant, produces more hydroxyl radicals (·OH) with α-Ni(OH)$_2$ when passed into the liquid, which enhances the α-Ni(OH)$_2$ photocatalytic degradation of the fracturing flowback liquid. The chemical oxygen demand (COD) degradation rate of group B is 18.73%, which is 2.41% higher than that of group 1, reflecting the synergistic effect of ozone on the α-Ni(OH)$_2$ photocatalytic degradation of the fracturing flowback liquid.

Figure 9 shows that the photocatalytic performance of the prepared α-Ni(OH)$_2$ photocatalyst first increases and then decreases with an increase in the amount of α-Ni(OH)$_2$. When 0.1 and 0.3 g of α-Ni(OH)$_2$ are used, the degradation rates of the hydroxypropyl gel breaker are higher, at 18.18% and 18.65%, respectively, while the absorbance and turbidity also decrease significantly. If the dosage of α-Ni(OH)$_2$ is relatively high, the degradation effect decreases. It was
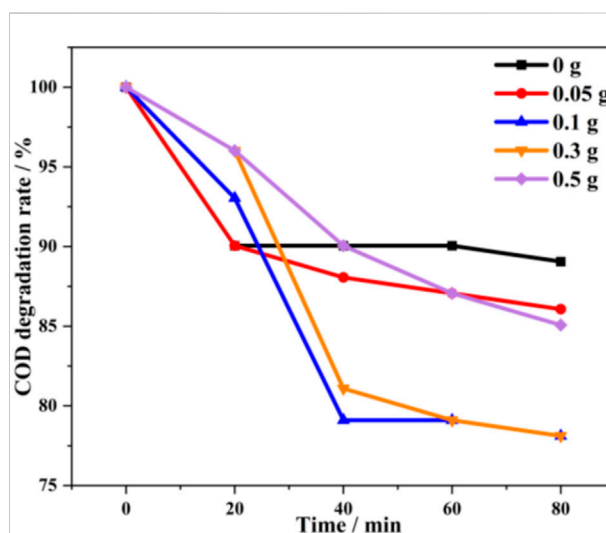
FIGURE 9
Comparison of different α-Ni(OH)$_2$ dosages for the photocatalytic degradation of hydroxypropyl gel breaker.

presumed that this is because the α-Ni(OH)$_2$ is a solid powder that is insoluble in water. An excessive amount makes the reaction sample liquid cloudy and unclear, which affects the light absorption rate. This, in turn, affects the photocatalytic effect. Therefore, preferentially, 0.1 or 0.3 g of α-Ni(OH)$_2$ is used in subsequent experiments.

As the reaction progresses, the degradation rate of the hydroxypropyl gel breaker with the prepared α-Ni(OH)$_2$ photocatalyst gradually slows down. At 40 min, the COD reduction in group 2 accounts for 87.50% of the final COD reduction at 120 min. The COD reduction in group 3 accounts for 82.61% of the final COD reduction at 120 min, and group 2 approaches the degradation limit at approximately 40 min, which is more obvious than that in group 3. In summary, a
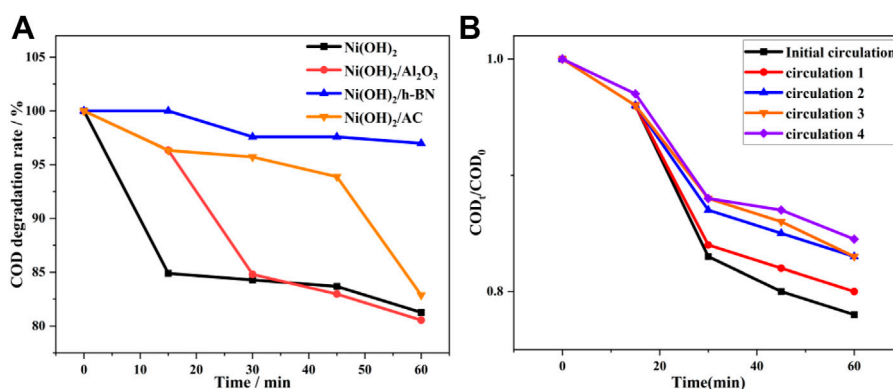
FIGURE 10
(A) Comparison of the performances of four photocatalysts for the degradation of fracturing flowback fluid; and **(B)** Cycling runs in the photocatalytic degradation of α-Ni(OH)₂/nano-Al₂O₃.
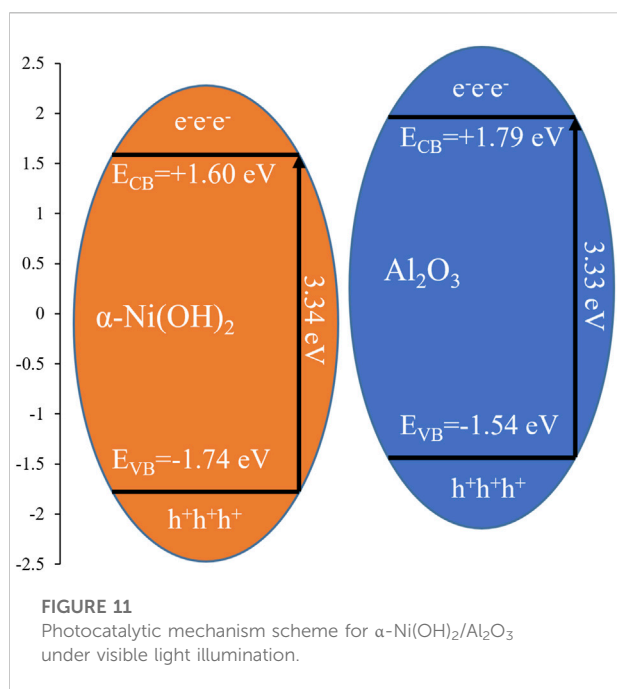
FIGURE 11
Photocatalytic mechanism scheme for α-Ni(OH)$_2$/Al$_2$O$_3$ under visible light illumination.

reaction fluid, the effects of the four photocatalysts on the degradation of the fracturing flowback fluid were compared, and the experimental results are shown in Figure 10A.

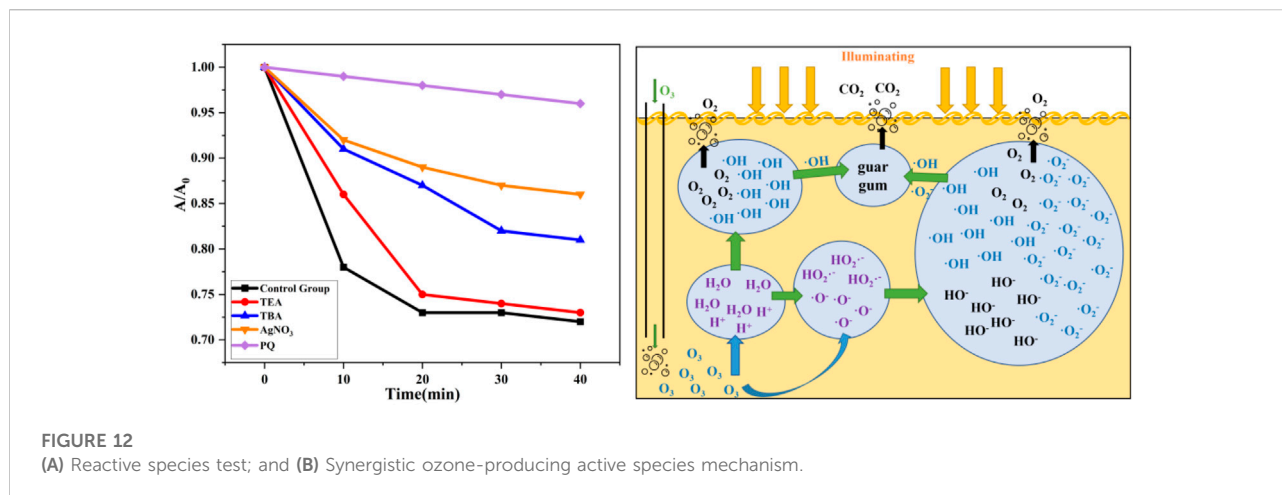The results show that the α-Ni(OH)$_2$, α-Ni(OH)$_2$/nano-Al$_2$O$_3$, and α-Ni(OH)$_2$/AC all yield effects over the reaction time when the four photocatalysts are used to degrade the underground fracturing flowback fluid, with COD degradation rates of 18.73%, 19.45%, and 17.13%, respectively, along with significant reductions in turbidity and spectrophotometry. The α-Ni(OH)$_2$/h-BN barely produces any effect, and the COD degradation rate is only 3.02%.This results from the presence of h-BN adhering to the α-Ni(OH)$_2$ surface in a crumbly form, affecting the adsorption efficiency of degradates which resulted in the degradation of α-Ni(OH)$_2$/h-BN. In summary, considering the degradation rate and efficiency, it was found that the α-Ni(OH)$_2$/nano-Al$_2$O$_3$ composite photocatalyst had the highest photocatalytic degradation activity for the fracturing flowback fluid (Figure 11).

The stability of a photocatalyst is an important performance indicator. Therefore, five repeated experiments were conducted for the selected α-Ni(OH)$_2$/Al$_2$O$_3$. The modified photocatalysts were photocatalytically stable (Figure 10B).

dosage of 0.1 g of α-Ni(OH)$_2$ and a reaction time of 40 min are the preferred experimental conditions.

Optimal performances of photocatalysts for fracture flowback fluid degradation

The α-Ni(OH)$_2$ and three types of carriers were used to degrade 150 ml of the fracturing flowback fluid, with samples taken every 15 min on average, and each group was sampled four times in turn (Table 3). Combined with the initial data of the

Mechanisms

Ammonium persulfate gel breaker systems are often used in actual field applications. Ammonium persulfate mainly relies on the decomposition of persulfate in water to produce acid and strongly oxidized radicals to destroy the acetal structure of the crosslinking gum fracturing fluid, thereby causing the gel to break (Jiang et al., 2012). The hydrolysis rate is positively correlated with temperature, and the decomposition half-life, $t_{1/2}$, is as long as 8 h at

FIGURE 12
(A) Reactive species test; and **(B)** Synergistic ozone-producing active species mechanism.

70°C (Wu, 2000), with amount of hydrolyze for gum-breaking, covalent intermediates, and stable intermediates remaining in the fracturing flowback fluid.

$$(NH_4)_2S_2O_8 + H_2O \rightarrow (NH_4)_2SO_4 + H_2SO_4 + \cdot O$$
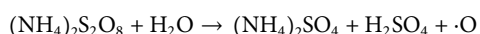
Compared with pure α-Ni(OH)$_2$, the prepared α-Ni(OH)$_2$/Al$_2$O$_3$ composite sample has lower electron-hole complexation rate and higher carrier transport efficiency, and its degradation rate of fracture rejection fluid COD can be enhanced by 18.7% under simulated sunlight irradiation.

Unlike the degradation of guanidine gum by ammonium persulfate, which is commonly used in oil and gas fields, the mechanism of the photocatalytic degradation of guanidine gum needs to be further clarified; therefore, active species capture experiments were conducted. As shown in Figure 12A, the active species and catalytic efficacy produced by the photocatalyst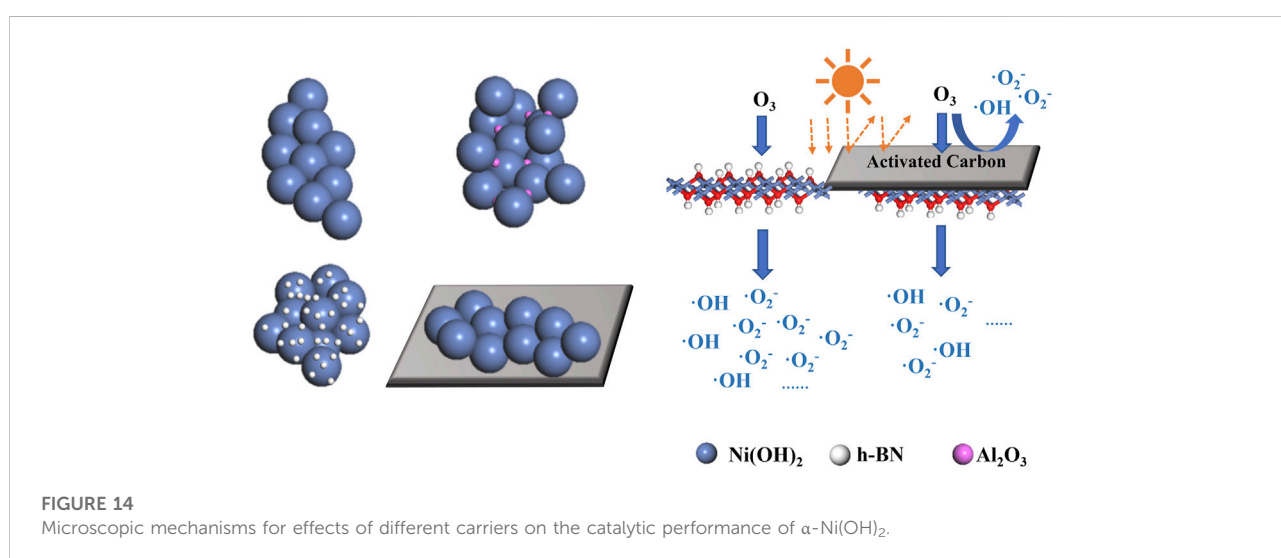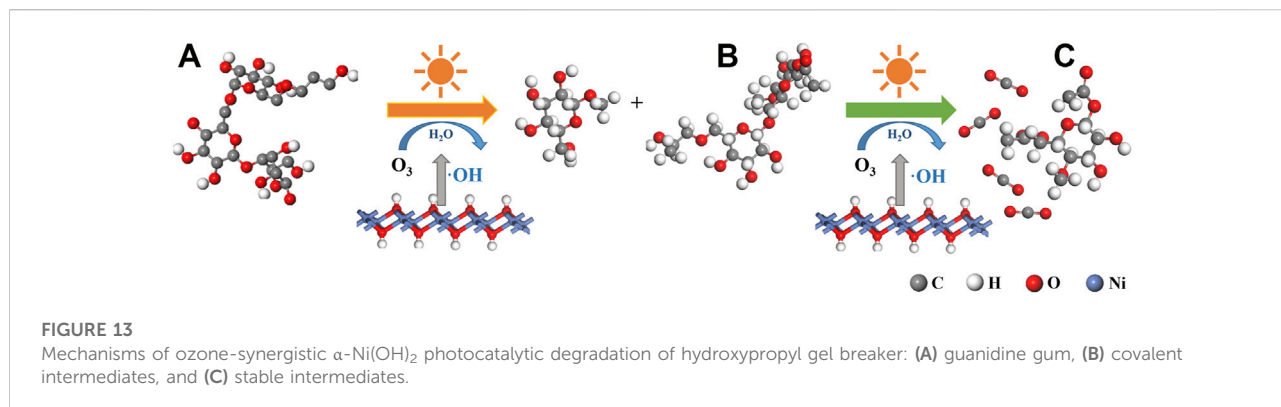 during the photocatalytic process are detected by adding silver nitrate to capture photogenerated electrons, tert-butyl alcohol to capture hydroxyl radicals, triethanolamine to capture photogenerated holes, andbenzyl kun to capture superoxide radicals in the differentreaction groups. Then, 1 mmol of trapping agent was added with 0.02 g of α-Ni(OH)$_2$/nano-Al$_2$O$_3$ photocatalyst to 150 ml of hydroxypropylguanidine gum breaking solution and stirred with a magnetic stirrer for 30 min in the dark to allow the adsorption to reach adsorption–desorption equilibrium. The degradation rate of the hydroxypropylguanidine gum-breaking solution was measured after a period of time using visible light irradiation with a 300 W xenon lamp to determine whether the photocatalytic activity of the α-Ni(OH)$_2$/nano-Al$_2$O$_3$ photocatalyst was inhibited by the addition of a trapping agent to investigate the photocatalytic mechanism.

Compared to the control experiment, the addition of each inhibitory active species agent led to a decrease in the

degradation rate, indicating that the α-Ni(OH)$_2$/nano-Al$_2$O$_3$ photocatalyst could generate superoxide radicals (·O$_2^-$), hydroxyl radicals (·OH), photogenerated electrons (e$^-$), and photogenerated holes (h$^+$) in different degrees under the synergistic catalytic effect of ozone, promoting the degradation of hydroxypropylguanidine gum and its broken gum residues. Meanwhile, the ozone itself decomposes in the aqueous phase to produce HO$_2^-$ and O$^-$, which in turn produces ·O$_2^-$ and·OH promoting the decomposition of the macromolecular guanidine glue-breaking substances. The effects of the active substances have the following order: ·O$_2^-$ > e$^-$ > OH > h$^+$. Ozone is adsorbed onto the active sites on the catalyst surface, which promotes the catalytic decomposition of the ozone and generates hydroxyl radicals. The hydroxyl radicals can be physically adsorbed on the catalyst surface or diffuse back to the main solution (Figure 12B).

In this study, ozone combined with α-Ni(OH)$_2$ and its composite materials are used for the photocatalytic degradation of hydroxypropyl gel breakers. The electrons transferred by the valence change in α-Ni(OH)$_2$ can effectively promote ozone decomposition to produce ·OH and ·O$_2^-$ under the effect of light (Li et al., 2021). The resulting ·OH and ·O$_2^-$ are present on the β-1,4-glycosidic bond of the main chain of the hydroxypropyl gum molecule (Hilge et al., 1998) Figure 13A, leading to its breakage and the formation of a covalent intermediate (Figure 13B), while providing protons through acid catalysis to form a stable intermediate (Figure 13C).

The adsorption of pollutants and the number of reaction sites during the catalytic reaction are key factors affecting the catalytic activity (Zhang et al., 2021). α-Ni(OH)$_2$ monolithic spheres are not usually found in the form of single particles but rather in an irregular morphological bulk accumulation, which leads to a reduction in the

FIGURE 13
Mechanisms of ozone-synergistic α-Ni(OH)₂ photocatalytic degradation of hydroxypropyl gel breaker: **(A)** guanidine gum, **(B)** covalent intermediates, and **(C)** stable intermediates.

FIGURE 14
Microscopic mechanisms for effects of different carriers on the catalytic performance of α-Ni(OH)₂.

specific surface area of the sphere-like α-Ni(OH)₂. Through the carrier composite, nano-Al₂O₃ can be successfully inserted between the spheres of α-Ni(OH)₂. The support effect changes the stacking morphology, and there are more adsorption and reaction sites for pollutants, which maximizes the catalytic reaction efficiency among the three types of carriers. In addition, this study compared 1:1 carrier-catalyst composites to α-Ni(OH)₂ without a carrier. The α-Ni(OH)₂/AC has a significantly larger specific surfac area because the AC is a large layer that blocks part of the light and affects the light range. Second, because the AC has a certain role in catalyzing O₃ into·OH, it consumes part of the O₃ to worsen the synergistic catalytic effect. In addition, the larger AC structure cannot enter between the α-Ni(OH)₂ spheres, and the larger specific surface is only due to the larger specific surface of the AC itself, thus reducing the catalytic efficiency. The h-BN reduces the specific surface area and exhibits the lowest catalytic degradation

efficiency owing to its excellent adhesion on the pompom surface (Figure 14).

Conclusion

In summary, ozone showed an effective synergy with α-Ni(OH)₂ to generate·OH/·O₂⁻ and improve the photocatalytic efficiency. The experimental results for the degradation of a hydroxypropyl gel breaker showed that the final photocatalytic degradation rate of α-Ni(OH)₂ in synergy with ozone reached 18.73%, indicating good photocatalytic activity. In addition, introducing the three loading materials changed the layer structure and pore size of α-Ni(OH)₂, creating more adsorption sites for pollutants, thus improving the photocatalytic performance. Among these, nano-Al₂O₃ had the most significant effect on the layer spacing, with the best photocatalytic degradation rate of 19.45% for the organic

pollutants in the fracturing flowback fluid. Because the final experimental sample was selected at 40 min, the final rate for the degradation of the fracturing fluid using α-Ni(OH)$_2$/nano-Al$_2$O$_3$ could be calculated to be 22.23%. In combination with a series of structural performance tests, it was shown that Al$_2$O$_3$ could support α-Ni(OH)$_2$ pellets and increase the comparative catalyst area, while enhancing the O$_3$ adsorption sites and providing better electron migration pathways. This study could effectively provide a novel green method for treating fracturing flowback fluids.

Data availability statement

The raw data supporting the conclusion of this article will be made available by the authors, without undue reservation.

Author contributions

HY and XT are responsible for the overall idea of the paper. RL and XT are responsible for experiments and paper data processing and so on. XL, PZ, and YG are responsible for organizing pictures. All authors contributed to the article and approved the submitted version.

Conflict of interest

Author PZ was employed by the company West-East Gas Transmission Branch of State Pipeline Group United Pipeline Co.

The remaining authors declare that the research was conducted in the absence of any commercial or financial relationships that could be construed as a potential conflict of interest.

Publisher's note

All claims expressed in this article are solely those of the authors and do not necessarily represent those of their affiliated organizations, or those of the publisher, the editors and the reviewers. Any product that may be evaluated in this article, or claim that may be made by its manufacturer, is not guaranteed or endorsed by the publisher.

References

Agustina, T. E., Ang, H. M., and Vareek, V. K. (2006). A review of synergistic effect of photocatalysis and ozonation on wastewater treatment. *J. Photochem. Photobiol. C Photochem. Rev.* 6 (4), 264–273. doi:10.1016/j.jphotochemrev.2005.12.003

Ahmed, Saber (2012). Impact of operating conditions and recent developments in heterogeneous photocatalytic water purification process. *Crit. Rev. Environ. Sci. Technol.* 42 (6), 601–675. doi:10.1080/10643389.2010.526492

Aminto, A., and Olson, M. S. (2012). Four-compartment partition model of hazardous components in hydraulic fracturing fluid additives. *J. Nat. Gas Sci. Eng.* 7, 16–21. doi:10.1016/j.jngse.2012.03.006

Carp, O., Huisman, C. L., and Reller, A. (2004). Photoinduced reactivity of titanium dioxide. *Prog. Solid State Chem.* 32 (1-2), 33–177. doi:10.1016/j.progsolidstchem.2004.08.001

Chang, H., Liu, J., Dong, Z., Wang, D., Xin, Y., Jiang, Z., et al. (2021). Enhancement of photocatalytic degradation of polyvinyl chloride plastic with Fe2O3 modified AgNbO3 photocatalyst under visible-light irradiation. *Chin. J. Struct. Chem.* 40 (12), 1595–1603. doi:10.14102/j.cnki.0254-5861.2011-3217

Chen, Y., Xu, Y., Lin, D., Luo, Y., Xue, H., and Chen, Q. (2020). Insight into superior visible light photocatalytic activity for degradation of dye over corner-truncated cubic Ag2O decorated TiO2 hollow nanofibers. *Chin. J. Struct. Chem.* 39 (3), 588–597.

Dhanalakshmi, K. B., Anandan, S., Madhavan, J., and Maruthamuthu, P. (2008). Photocatalytic degradation of phenol over TiO2 powder: The influence of peroxomonosulphate and peroxodisulphate on the reaction rate. *Sol. Energy Mat. Sol. Cells* 92 (4), 457–463. doi:10.1016/j.solmat.2007.10.009

Dunia, A. A. F., Amal, M. A. M., Roua, M. A., and Noorah, A. A. (2021). Facile synthesis and characterization of CeO2-Al2O3 nano-heterostructure for enhanced visible-light photocatalysis and bactericidal applications. *Colloid Interface Sci. Commun.* 41, 100375. doi:10.1016/j.colcom.2021.100375

Fu, J., Wang, X., Ma, Z., Hao, W., Wang, L., Wang, Z., et al. (2019). Photocatalytic ultrafiltration membranes based on visible light responsive photocatalyst: A review. *Desalination Water Treat.* 168 (0), 42–55. doi:10.5004/dwt.2019.24403

Gao, X. Y., Zeng, D. Q., Yang, J. G., Ong, W. J., Fujita, T., He, X. L., et al. (2021). Ultrathin Ni(OH)2 nanosheets decorated with Zn0.5Cd0.5S nanoparticles as 2D/0D heterojunctions for highly enhanced visible light-driven photocatalytic hydrogen evolution. *Chin. J. Catal.* 42 (7), 1137–1146. doi:10.1016/s1872-2067(20)63728-7

Hall, D. S., Lockwood, D. J., Bock, C., and Macdougall, B. R. (2015). Nickel hydroxides and related materials: A review of their structures, synthesis and properties. *Proc. R. Soc. A* 471 (2174), 20140792–20140865. doi:10.1098/rspa.2014.0792

Hilge, M., Gloor, S. M., Rypniewski, W., Sauer, O., Pointek, K., Zimmermann, W., et al. (1998). High-resolution native and complex structures of thermostable β-mannanase from Thermomonospora fusca – substrate specificity in glycosyl hydrolase family 5. *Structure* 6 (11), 1433–1444. doi:10.1016/s0969-2126(98)00142-7

Huang, Y., Mao, J., Qian, Q., Xue, H., and Liu, Y. (2021). Study on the different photocatalytic performances for tetracycline hydrochloride degradation of p-block metal composite oxides Sr1.36Sb2O6 and Sr2Sb2O7. *Chin. J. Struct. Chem.* 40 (3), 394–402. doi:10.14102/j.cnki.0254-5861.2011-3105

Jia, D., Gao, H., Dong, W., Fan, S., Dang, R., and Wang, G. (2017). Hierarchical α-Ni(OH)2 composed of ultrathin nanosheets with controlled interlayer distances and their enhanced catalytic performance. *ACS Appl. Mat. Interfaces* 9 (24), 20476–20483. doi:10.1021/acsami.7b02100

Jiang, H. Y., Wang, S. B., Guo, J. C., and Yao, Y. (2012). Research on improving decomposition rate of ammonium persulfate in condition of low temperature. *Zuanjingye Yu Wanjingye* 29 (1), 77–78.

Kim, K., Kim, M. J., and Kim, J. H. (2014). Enhancement of the thermal and mechanical properties of a surface-modified boron nitride-polyurethane composite. *Polym. Adv. Technol.* 25 (8), 791–798. doi:10.1002/pat.3291

Lee, J. T., Tseng, H. H., and Wey, M. Y. (2022). Excellent dispersion of solar light responsive photocatalyst in the different polymer films for easy recycling and sustainable hydrogen production. *Sol. Energy* 231, 949–957. doi:10.1016/j.solener.2021.12.041

Lee, J. W., Ko, J. M., and Kim, J. D. (2011). Hierarchical microspheres based on α-Ni(OH) 2 nanosheets intercalated with different anions: Synthesis, anion exchange, and effect of intercalated anions on electrochemical capacitance. *J. Phys. Chem. C* 115 (39), 19445–19454. doi:10.1021/jp206379h

Li, J. C., Lei, Z. D., Tang, H. Y., Tian, C. B., and Gong, B. (2016). Efficient evaluation of gas recovery enhancement by hydraulic fracturing in unconventional reservoirs. *J. Nat. Gas Sci. Eng.* 35 (A), 873–881. doi:10.1016/j.jngse.2016.08.067

Li, K., Rimmer, S. M., Liu, Q. F., and Zhang, Y. M. (2019). Micro-Raman spectroscopy of microscopically distinguishable components of naturally graphitized coals from central hunan province, China. *Energy fuels.* 33 (2), 1037–1048. doi:10.1021/acs.energyfuels.8b04065

Li, X. D., Ding, R., Shi, W., Xu, Q. L., Ying, D. F., Huang, Y. F., et al. (2018). Hierarchical porous Co(OH)F/Ni(OH)2: A new hybrid for supercapacitors. *Electrochim. Acta* 265, 455–473. doi:10.1016/j.electacta.2018.01.194

Li, Y., Zhu, J. Y., Hu, J. Y., Li, W., Li, Y., Zhang, D., et al. (2021). Catalytic ozonation for effective degradation of aniline by sulfur-doped copper–nickel bimetallic oxide in aqueous solution. *J. Environ. Chem. Eng.* 9 (1), 104953. doi:10.1016/j.jece.2020.104953

Li, Z. C., Han, J., Fan, L., Wang, M. G., Tao, S. Y., and Guo, R. (2015). The anion exchange strategy towards mesoporous α-Ni(OH)2 nanowires with multinanocavities for high-performance supercapacitors. *Chem. Commun.* 51 (15), 3053–3056. doi:10.1039/c4cc09225b

Liu, D., Fan, M., Yao, L., Zhao, X., and Wang, Y. (2010). A new fracturing fluid with combination of single phase microemulsion and gelable polymer system. *J. Petroleum Sci. Eng.* 73 (3-4), 267–271. doi:10.1016/j.petrol.2010.07.008

Mekki, M. B., Djouadi, M. A., Mortet, V., Guiot, E., Nouet, G., Mestres, N., et al. (1999). Synthesis and characterization of c-BN films prepared by ion beam assisted deposition and triode sputtering. *Thin Solid Films* 355-356, 89–95. doi:10.1016/s0040-6090(99)00509-x

Meng, A., Wu, S., Cheng, B., Yu, J., and Xu, J. (2018). Hierarchical TiO2/Ni(OH) 2 composite fibers with enhanced photocatalytic CO2 reduction performance. *J. Mat. Chem. A Mat.* 6 (11), 4729–4736. doi:10.1039/c7ta10073f

Mohammad, M., Siegfried, M., and Detlev, M. (2012). Synergistic effect of the combination of immobilized TiO2, UVA and ozone on the decomposition of dichloroacetic acid. *J. Environ. Sci. Health, Part A Toxic/Hazardous Subst. Environ. Eng.* 47 (8), 1073–1081. doi:10.1080/10934529.2012.668026

Mutalib, M. A., Aziz, F., Jamaludin, N. A., Yahya, N., Isamail, A. F., Mohamed, M. A., et al. (2018). Enhancement in photocatalytic degradation of methylene blue by LaFeO3-GO integrated photocatalyst-adsorbents under visible light irradiation. *Korean J. Chem. Eng.* 35 (2), 548–556. doi:10.1007/s11814-017-0281-0

Nien, Y. H., Chen, J. F., Fang, C. Y., and Liu, M. S. (2022). Preparation of ZrO2/graphene oxide/TiO2 composite photocatalyst and its studies on decomposition of organic matter. *J. Compos. Sci.* 6 (9), 9. doi:10.3390/jcs6010009

Rajendiran, R., Muthuchamy, N., Park, K. H., Li, O. L., Kim, H. J., and Prabakar, K. (2020). Self-assembled 3D hierarchical MnCO3/NiFe layered double hydroxides as a superior electrocatalysts for the oxygen evolution reactions. *J. colloid interface Sci.* 566, 224–233. doi:10.1016/j.jcis.2020.01.086

Ran, J., Yu, J., and Jaroniec, M. (2011). Ni(OH)2 modified CdS nanorods for highly efficient visible-light-driven photocatalytic H2 generation. *Green Chem.* 13 (10), 2708–2713. doi:10.1039/C1GC15465F

Shi, X., Wang, P. Q., Wang, L., Bai, Y., Xie, H. Q., Zhou, Y., et al. (2019). Change in photocatalytic NO removal mechanisms of ultrathin BiOBr/BiOI via NO3– adsorption. *Appl. Catal. B Environ.* 243, 322–329. doi:10.1016/j.apcatb.2018.10.037

Shi, X., Wang, P. Q., Wang, L., Bai, Y., Xie, H. Q., Zhou, Y., et al. (2018). Few layered BiOBr with expanded interlayer spacing and oxygen vacancies for efficient decomposition of real oil field produced wastewater. *ACS Sustain. Chem. Eng.* 6 (11), 13739–13746. doi:10.1021/acssuschemeng.8b01622

Shi, X., Wang, P. Q., Zhang, K., and Li, X. (2019). Ultrathin bismuth oxyhalides solid solution nanosheets with oxygen vacancies for enhanced selective photocatalytic NO removal process. *J. Mat. Sci. Mat. Electron.* 30 (19), 17828–17837. doi:10.1007/s10854-019-02134-x

Sidiras, D., Batzias, F., Schroeder, E., Ranjan, R., and Tsapatsis, M. (2011). Dye adsorption on autohydrolyzed pine sawdust in batch and fixed-bed systems. *Chem. Eng. J.* 171 (3), 883–896. doi:10.1016/j.cej.2011.04.029

Tretyachenko, E. V., Gorokhovsky, A. V., Yurkov, G. Y., Fedorov, F. S., Vikulova, M. A., Lovaleva, D. S., et al. (2014). Adsorption and photo-catalytic properties of layered lepidocrocite-like quasi-amorphous compounds based on modified potassium polytitanates. *Particuology* 17 (6), 22–28. doi:10.1016/j.partic.2013.12.002

Wang, H. Y., Hsu, Y. Y., Chen, R., Chan, T. S., Chen, H. M., and Liu, B. (2015). Oxygen evolution reaction: Ni3+-Induced formation of active NiOOH on the spinel Ni-Co oxide surface for efficient oxygen evolution reaction (adv. Energy mater. 10/2015). *Adv. Energy Mat.* 5 (10), 1500091. doi:10.1002/aenm.201570058

Wu, J. P. (2000). Low temperature fracturing fluid gel breaking technology for stimulation of shallow gas reservoirs. *Drill. Technol.* (5), 79–82.

Yan, Z., Yu, X., Zhang, Y., Jia, H., Sun, Z., and Du, P. (2014). Enhanced visible light-driven hydrogen production from water by a noble-metal-free system containing organic dye-sensitized titanium dioxide loaded with nickel hydroxide as the cocatalyst. *Appl. Catal. B Environ.* 160-161, 160173–161178. doi:10.1016/j.apcatb.2014.05.017

Yang, D. J., Liu, H. W., Zheng, Z. F., Yuan, Y., Zhao, J. C., Waclawik, E. R., et al. (2009). An efficient photocatalyst structure: TiO2(B) nanofibers with a shell of anatase nanocrystals. *J. Am. Chem. Soc.* 131 (49), 17885–17893. doi:10.1021/ja906774k

You, Q., Wang, H., Zhang, Y., Liu, Y. F., Fang, J. C., and Dai, C. L. (2018). Experimental study on spontaneous imbibition of recycled fracturing flow-back fluid to enhance oil recovery in low permeability sandstone reservoirs. *J. Petroleum Sci. Eng.* 166, 375–380. doi:10.1016/j.petrol.2018.03.058

Yu, J., Hai, Y., and Cheng, B. (2011). Enhanced photocatalytic H2-production activity of TiO2 by Ni(OH)2 cluster modification. *J. Phys. Chem. C* 115 (11), 4953–4958. doi:10.1021/jp111562d

Zhang, A., Zhang, R. Y., Fei, L., Zhu, J. C., Cao, Y. H., Zhang, Q., et al. (2021). Tunable microstructure of α-Ni(OH)2 for highly-efficient surface adsorbates activation to promote catalytic NO oxidation. *Chem. Eng. J.* 425, 130663. doi:10.1016/j.cej.2021.130663